Earth and Planetary Science Letters 488 (2018) 126–133

Contents lists available at ScienceDirect

Earth and Planetary Science Letters

www.elsevier.com/locate/epsl

The revised tectonic history of Tharsis

Sylvain Bouley [a,*], David Baratoux [b,c], Nicolas Paulien [a], Yves Missenard [a], Bertrand Saint-Bézar [a]

[a] GEOPS – Géosciences Paris Sud, Univ. Paris-Sud, CNRS, Université Paris-Saclay, Rue du Belvédère, Bât. 504-509, 91405 Orsay, France
[b] Geosciences Environnement Toulouse, IRD, Université de Toulouse, & CNRS UMR 5563, 14 Avenue Edouard Belin, 31400, Toulouse, France
[c] Institut Fondamental d'Afrique Noire Cheikh Anta Diop, Dakar, Senegal

ARTICLE INFO

Article history:
Received 11 December 2017
Received in revised form 7 February 2018
Accepted 12 February 2018
Available online 26 February 2018
Editor: F. Moynier

Keywords:
Mars
Tharsis
tectonic

ABSTRACT

Constraining the timing of the emplacement of the volcano-tectonic province of Tharsis is critical to understanding the evolution of mantle, surface environment and climate of Mars. The growth of Tharsis had exerted stresses on the lithosphere, which were responsible for tectonic deformation, previously mapped as radial or concentric faults. Insights into the emplacement history of Tharsis may be gained from an analysis of the characteristics and ages of these tectonic features. The number, total length, linear density of extensional or compressional faults in the Tharsis region and deformation rates are reported for each of the following 6 stages: Early and Middle Noachian (stage 1); Late Noachian (stage 2); Early Hesperian (stage 3); Late Hesperian (stage 4), Early Amazonian (stage 5) and Middle Amazonian to Late Amazonian (stage 6). 8571 Tharsis-related tectonic features (radial or concentric to the center of Tharsis) were assigned to one of these periods of time based on their relationship with stratigraphic units defined in the most recent geological map. Intense faulting at Tempe Terra, Claritas and Coracis Fossae and Thaumasia Planum confirms that tectonic deformation started during the Noachian. However, we report a peak in both compressive and extensive rates of deformation during the Early Hesperian whereas the quantitative indicators for compressional and extensional tectonics vary within less than one order of magnitude from the Late Noachian to the Late Hesperian. These observations indicate a protracted growth of Tharsis during the first quarter of Mars evolution and declining from 3 Gyrs ago.

1. Introduction

The Tharsis dome is the largest volcano-tectonic center on Mars and in the solar system. It is one of the most impressive crustal expressions of the internal dynamics of Mars. Its growth was likely associated with the release of large volumes of volcanic gases having dramatic consequences on climatic evolution and surface environment during a period of time when Mars was habitable (Ehlmann et al., 2016). The growth of Tharsis and the inferred mantle plume exerted stresses on the martian lithosphere. Crustal stresses have resulted in the formation of tectonic features, mapped as compressional or extensional faults, radial or concentric to the center of the dome. The chronology of crustal deformation was elaborated from stratigraphic and cross-cutting relationships and from the number of tectonic features affecting the geological units of various ages in the Tharsis region (e.g., Scott and Tanaka, 1986; Anderson et al., 2001; Dohm et al., 2001; Carr and Head, 2010). From these observations, the major growth episodes of Tharsis are considered to take place during the Middle and Late Noachian Epochs (Phillips et al. 2001; Anderson et al., 2001; Viviano-Beck et al., 2017). The conclusion that Tharsis was largely in place at the end of the Noachian is supported by the high number of tectonic features identified in Noachian terrains in the western equatorial region (Scott and Tanaka, 1986), Alba Patera (Tanaka, 1990), Olympus Mons (Morris and Tanaka, 1994), Valles Marineris (Witbeck et al., 1991), the Syria Planum (Tanaka and Davis, 1988), Tempe Terra and Ulysses Patera (Scott and Dohm, 1990), Alba Patera (Tanaka, 1990) and Thaumasia regions (Dohm and Tanaka, 1999) of Mars.

However, the ages of these different units have been recently revised from more recent and high-resolution imagery (Tanaka et al., 2014). For instance, Ceraunius Fossae, Tempe Terra or Syria Planum, initially assigned to the Noachian era, are now mapped as Early and Late Hesperian units (Tanaka et al., 2014). Moreover, the number of faults may be a meaningless proxy for deformation rates, since it treats a 1 km long fault as being equal to a 1000 km long fault (both of which exist on the surface of Mars in abundance). The number of faults is also sensitive to the resolution of

* Corresponding author.
E-mail address: sylvain.bouley@u-psud.fr (S. Bouley).

https://doi.org/10.1016/j.epsl.2018.02.019
0012-821X/

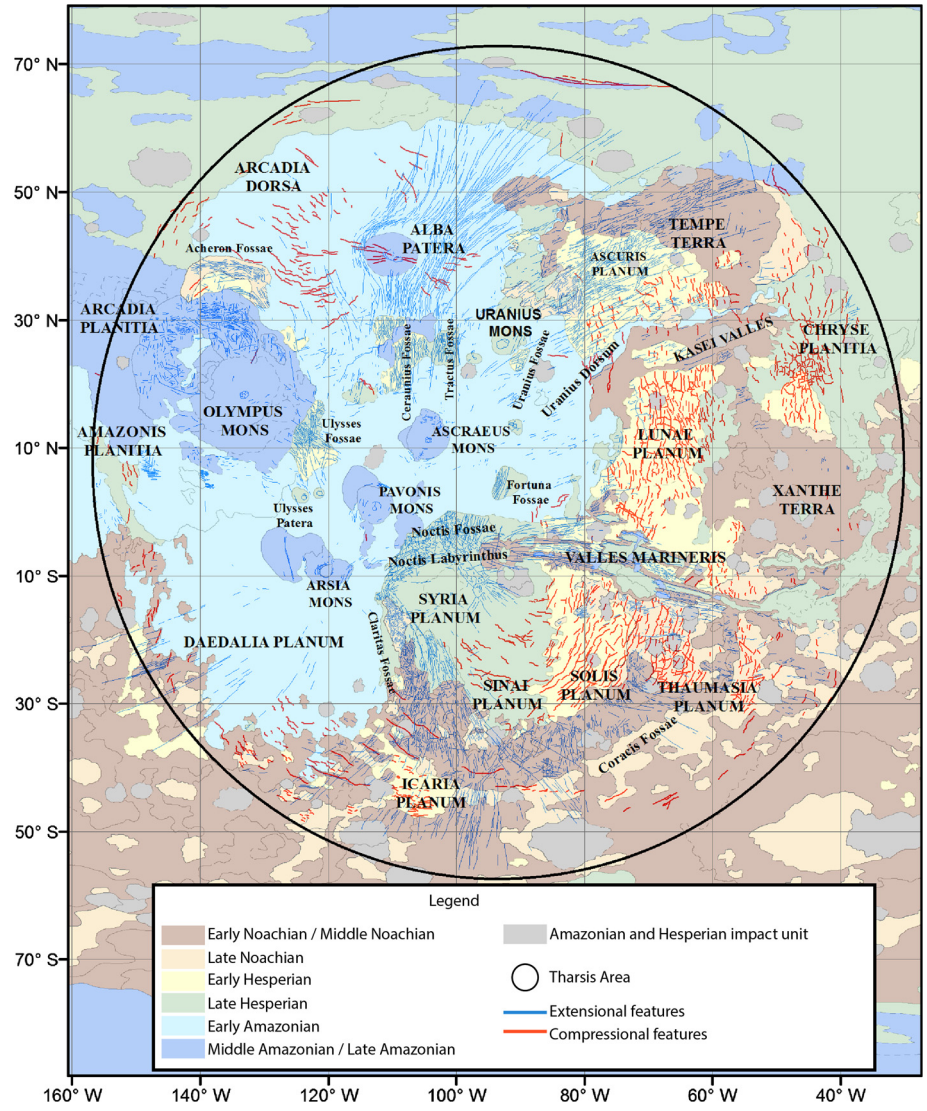

Fig. 1. Simplified geologic map from Tanaka et al. (2014). The different units are grouped into five stages: stage 1, Early and Middle Noachian; stage 2, Late Noachian; stage 3, Early Hesperian; stage 4, Late Hesperian; stage 5, Early Amazonian and stage 6, Middle Amazonian to Late Amazonian. The black ellipse shows the studied Tharsis area. Red lines (compressional) and blue lines (extensional) represent tectonic features from Knapmeyer et al. (2008). (For interpretation of the colors in the figure(s), the reader is referred to the web version of this article.)

the data, since many faults are segmented into numerous distinct but closely approaching segments that are likely interconnected in the subsurface.

The purpose of this paper is therefore to revisit the tectonic evolution of Tharsis using quantitative indicators, including fault length and density, that can be related more directly to the deformation rate as a function of time, which is itself related to changes in load intensity. These quantitative indicators are also estimated from the new geological map of this region (Tanaka et al., 2014), which differs significantly from the map used in earlier estimations.

Methodology and data sets

Many authors (Wise et al., 1979; Banerdt et al., 1982; Anderson et al., 2001) provide evidence of the radial nature of the stress field in the volcano-tectonic province of Tharsis. Anderson et al. (2001) suggested that the number of faults groups into 5 different stages was indicative of the intensity of volcano-tectonic activity and its evolution with time. Here we build on this approach and suggest that the growth of Tharsis may be deciphered from the characteristics and ages of tectonic features.

Tectonic features were previously mapped by Anderson et al. (2001) from Viking images, which are heterogeneous in terms of resolution and conditions of illuminations. For this study, we use a global inventory of Mars surface faults based on shaded relief maps from MOLA data (Knapmeyer et al., 2008). This catalog contains a total numbers of 14 835 faults, with 5146 thrust and 9689 normal faults, with a cumulative length of about 941 000 km. The Tharsis region is defined by an ellipse centered at 9°30′29″N and 98°15′26″W and encompasses 8571 tectonic elements of the catalog, including 1376 thrust faults and 7195 normal faults (Fig. 1). Grabens and rifts are bounded by normal faults that result from extensional stresses, and wrinkle ridges are formed by thrust faults that result from compressional stresses (Banerdt et al., 1992; Anderson et al., 2001). The fault catalog is a georeferenced layer loaded in the ArcGIS software.

The age of each fault is determined from stratigraphic and crosscutting relationships among the different geological units mapped by Tanaka et al. (2014) (Fig. 1). A fault appearing in several units of different ages is assigned to the age of the youngest unit affected by the fault. A fault affecting a single unit but having a similar orientation and morphology to faults occurring both

Table 1
Characteristics of extensional and compressional features for each stage.

	Stage 1	Stage 2	Stage 3	Stage 4	Stage 5	Stage 6	Total
Area (10^6 km^2)	9.4	3	4.5	7	13.8	5	42.7
Center of area				9°30′29″N–98°15′26″W			
Extensional							
Number of faults	1731 (24%)	854 (12%)	1308 (18%)	1185 (16.5%)	1197 (16.5%)	920 (13%)	7195
Density (10^{-4} faults/km^2)	1.84	2.84	2.9	1.7	0.9	1.84	
Cumulative length (km)	97463 (21%)	45521 (10%)	81093 (17.5%)	75879 (16.5%)	110318 (24%)	50279 (11%)	460555
Mean (km)	56	53	62	64	92	55	
σ	52	59	64	70	120	61	
Linear fault density (km/km^2)	0.010	0.015	0.018	0.011	0.008	0.010	
Compressional							
Number of faults	72 (5%)	254 (18.5%)	584 (42.5%)	287 (21%)	141 (10%)	38 (3%)	1376
Density (10^{-6} faults/km^2)	7.6	85	130	41	10.2	7.6	
Cumulative length (km)	6788 (6%)	17176 (16%)	40513 (38%)	22098 (20.5%)	15699 (14.5%)	5477 (5%)	107751
Mean (km)	94	67	69	77	111	144	
σ	71	46	54	49	71	188	
Linear fault density (km/km^2)	0.001	0.006	0.009	0.003	0.001	0.001	

in younger and older units is grouped together with those faults. In all cases, this method provides a maximum age of the fault: each fault could have a younger age than the units in which it is found. Tectonic features formed in an ancient period of time may be also reactivated at a later time. Such recent tectonic activity might not be recognized in our analysis. The intrinsic limitation of the stratigraphic method and the latter caveat both induce an underestimation of the intensity of recent tectonic activity.

Our classification contains 6 stages, inspired by the scheme described by Dohm and Tanaka (1999): Early and Middle Noachian (stage 1 – Units eNh, mNh, NHu); Late Noachian (stage 2 – Units lNh, lNv); Early Hesperian (stage 3 – Units eHh, eHv, eHt); Late Hesperian (stage 4 – Units lHv, lHt, Hto, Htu, Hve, lHvf, lHl), Early Amazonian (stage 5 – Units AHv, AHtu) and Middle Amazonian to Late Amazonian (stage 6 – Units Ave, lAv, lAvf, Aa).

Anderson et al. (2001) restricted their analysis to the number of features per stage as a proxy for tectonic activity. However, since the fault lengths are variable over several orders of magnitude, the number of fault may not be representative of the total amount of deformation and the fault length should be preferred (Scholz, 1982). Therefore, we explore here, in addition to the number of faults per stage, the total fault length, the linear fault density and the rate of deformation in each stage (Table 1). The total fault length (km) is defined as the cumulative length of faults in a given stage. The linear fault density (km/km^2) is the cumulative length of faults divided by the surface areas of units formed in that stage. The deformation rate (km/Myr/km^2) is estimated as the linear fault density divided by the duration of the stage. For all calculations, we have distinguished between extension faults and compressional faults. The durations of all stages are calculated from absolute age of boundaries of martian epochs proposed by Werner and Tanaka (2011) and derived according to fit of Ivanov (2001) and Hartmann (2005) SFD. The absolute age of Early Noachian–Pre-Noachian boundary, which is poorly constrained, is taken at 4.1 Ga (Carr and Head, 2010).

2. Data analysis and observations

2.1. Ages of extensional features

Fig. 2a shows a histogram of the total number of extensional faults identified by stage. 24% of the structures are formed in stage 1, 12% are formed in stage 2, 18% are associated with stage 3, 16.5% are formed in stage 4, 16.5% are formed in stage 5 and 13% in stage 6. The number of extensional faults is relatively homogeneous among the different time intervals. The Noachian features represent 36% of the total number of exposed ones (stage 1 and 2); 34.5% of the extensional features formed during the Hesperian (stage 3 and 4), and 29.5% during the Amazonian (stage 5 and 6). The total fault length (Fig. 2b) is maximum for the Early Amazonian period (stage 5). 21% of the total fault length (460 555 km) is associated with stage 1, 10% with stage 2, 17.5% with stage 3, 16.5% with stage 4, 24% with stage 5 and 11% with stage 5 (Fig. 2b). Fig. 2c shows a histogram of the number of extensional faults as a function of the fault length. For all stages, the majority of faults' lengths (65%) is comprised between 25 and 125 km with a mean length ranging from 53 km in stage 2 to 92 km in stage 4 (Table 1). Noachian (stage 1) to Late Hesperian (stage 4) and Middle/Late Amazonian faults (stage 6) are generally shorter than 400 km while Early Amazonian faults (stage 5) longer than 500 km are common and reach in some cases 1000 km. Despite these moderate differences between fault length distributions, there is a correlation between the number of faults and the cumulative fault length (Fig. 2b). The linear fault density ranges from 8×10^{-3} km/km^2 (stage 5) and 18×10^{-3} km/km^2 with a maximum for the Early Hesperian period (stage 3) (Fig. 2d).

Fig. 3 shows the evolution of the extensional deformation rate (blue) in the different stages. Whatever the chronological model, this rate is low during the Early/Middle Noachian period (stage 1) and the Late Hesperian/Amazonian periods (stage 4 to 6). It becomes higher during the Late Noachian and peaks during the Early Hesperian ($>10^{-4}$ km/Myr/km^2).

2.2. Ages of compressional features

Fig. 4a shows a histogram of the total number of compressional faults identified by stage. 5% of the structures are formed in stage 1, 18.5% in stage 2, 42.5% in stage 3, 21% in stage 4, 10% in stage 5 and 3% in stage 6. The number of compressional structures reaches a maximum for the Early Hesperian (stage 3). This same pattern is revealed from the total fault length (Fig. 4b). The total normal fault length of 107 751 km is distributed with 6% in stage 1, 16% in stage 2, 38% in stage 3, 20.5% in stage 4, 14.5% in stage 5 and 5% in stage 6 (Fig. 4b). A large peak is observed for the Early Hesperian period (stage 3). Fig. 4c shows a histogram of the number of compressional faults as a function of the fault length. The faults lengths are mostly comprised for all stages (78%) between 25 and 125 km with a mean length ranging from 67 km (stage 2) to 144 km (stage 6). The low number of faults and the presence of two long faults (360 and 411 km) explain the high mean length for the stage 1 faults. Most of the Noachian faults (stage 1 and 2) are relatively short (<200 km) while Early Hesperian to Early Amazonian faults (stage 3 to 5) larger than 200 km are common and reach in some cases 400 km. As for the case of

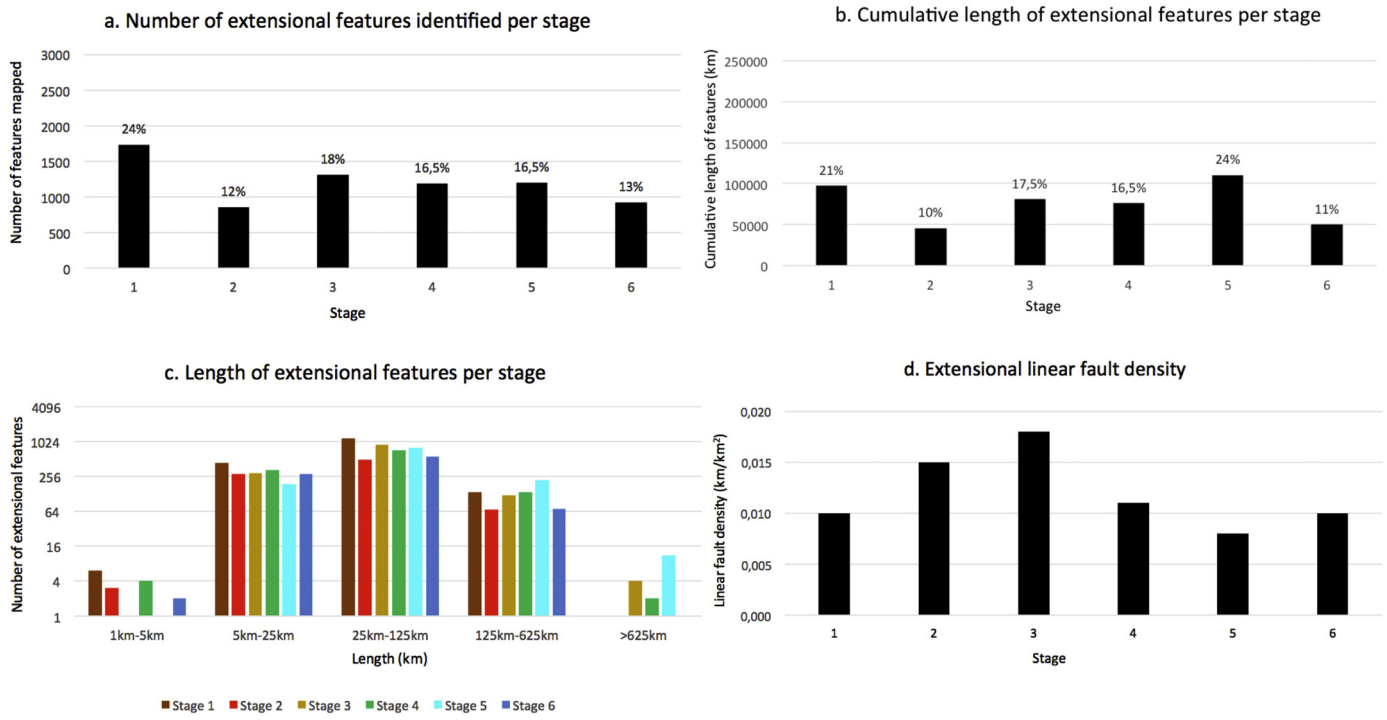

Fig. 2. (a) Number of extensional features identified per stage. (b) Cumulative length of extensional features per stage. (c) Histogram of the number of extensional faults versus fault length. (d) Linear extensional fault density per stage.

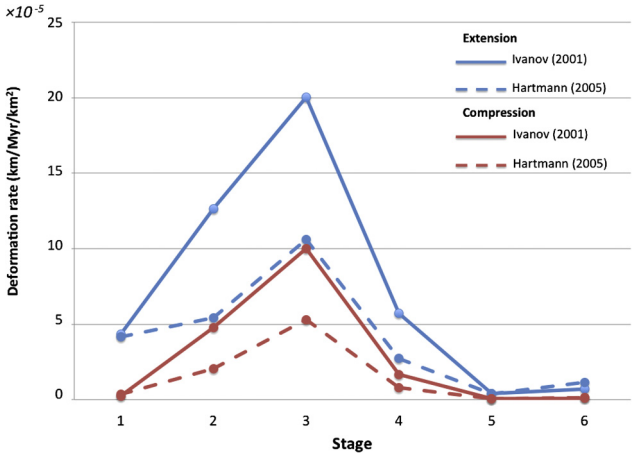

Fig. 3. Evolution of the extensional (red) and compressional deformation rate (blue) in the different stages. We calculated for each stage the deformation rate using total length divided by durations of the epochs and area. Durations of the epoch are calculated from absolute age of boundaries of martian epochs proposed by Werner and Tanaka (2011) and derived according to fit of Ivanov (2001) and Hartmann (2005) SFD.

extension, the number of faults and the cumulative fault length appear to be correlated (Fig. 4b). The linear fault density ranges from 10^{-3} km/km^2 in stage 1 to 9×10^{-3} km/km^2 for the Early Hesperian period (stage 3) (Fig. 4d).

Fig. 3 shows the evolution of the compressional deformation rate (blue) in the different stages. Whatever the chronological model, this rate is low during the Early/Middle Noachian period (stage 1) and the Late Hesperian/Amazonian periods (stage 4 to 6). It became higher during the Late Noachian and peaked during the Early Hesperian ($>5\times10^{-5}$ km/Myr/km^2).

3. Chronology of Tharsis tectonic activity

This section summarizes the chronology of Tharsis based on our revised ages of extensional and compressional activity. The inferred chronology of Tharsis is based on the assumption that the number, the total length of compressional or extensional features and the deformation rate in each stage reflect the amount of compressive or extensive deformation in each stage.

Anderson et al. (2001) disregarded the fact that the number of tectonic features is also influenced by the exposed surface area of units belonging to each classification stage. For instance, the number of Noachian features may be underestimated if most of the Noachian tectonic features are now buried under Early Hesperian or Early Amazonian terrain. We present here indicators that are normalized to the exposed areas of each unit, whereas we mention the non-normalized values for comparison with previous work (Figs. 2d and 3d). Examination of the relationships between exposed surface areas of each stage and number of features of total length suggests that the variable amount of exposed surface areas in each stage itself cannot explain the observed variations between each stage.

Stage 1

The Early/Middle Noachian epoch is characterized by low extensional deformation rate ($\sim 4 \times 10^{-5}$ km/Myr/km^2) occurring in two main regions located around the periphery of Tharsis: the northeast region with Tempe Terra and the south with Claritas and Coracis Fossae and Thaumasia Planum (Fig. 5). The majority of these normal faults are short structures. They are oriented N70 in Tempe Terra. The orientations of faults in Claritas and Coracis Fossae, and in Thaumasia Planum are more variable and range from N180 to N90. Some of these structures appear to form a radial pattern emanating approximately from the center of Tharsis (<300 km). Only few compressional features are observed in the south periphery of Tharsis.

Stage 2

The stage 2 (Late Noachian) is characterized both by extensional (between 1.25×10^{-4} and 5×10^{-5} km/Myr/km^2) and compres-

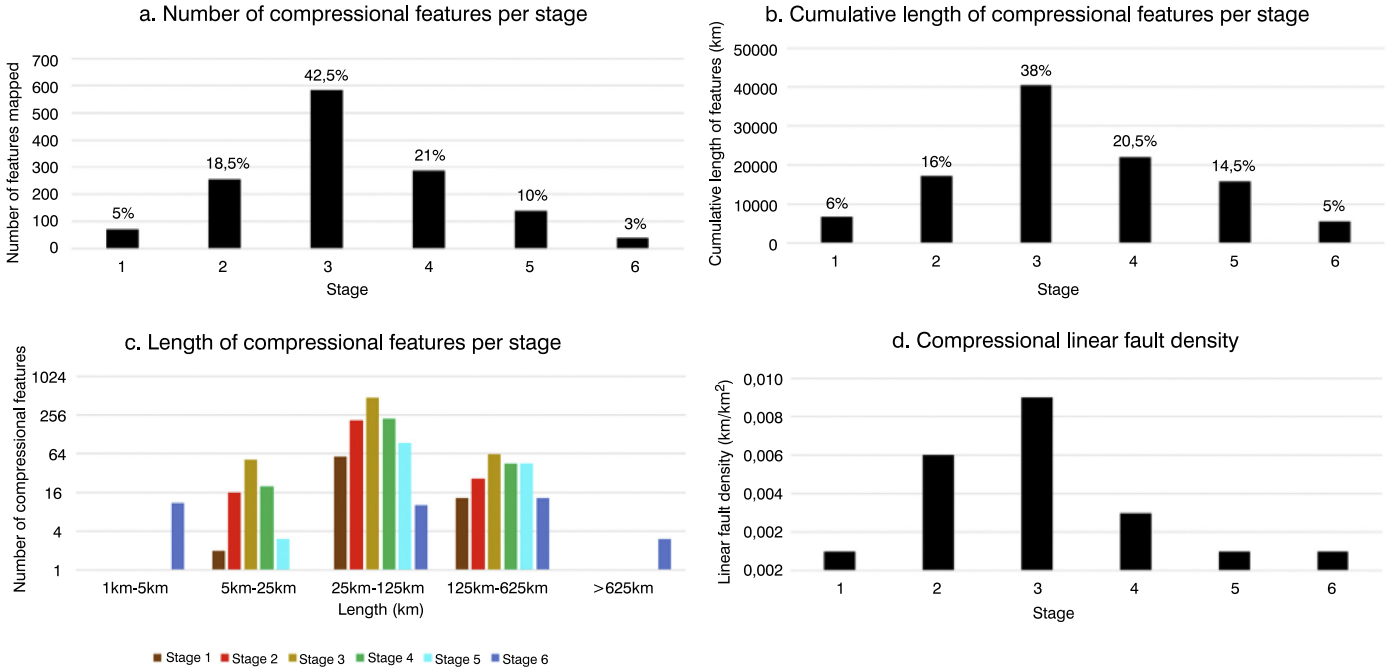

Fig. 4. (a) Number of compressional features identified per stage. (b) Cumulative length of compressional features per stage. (c) Histogram of the number of compressional faults versus fault length. (d) Linear compressional fault density per stage.

sional (between 2×10^{-5} and 4.7×10^{-5} km/Myr/km^2) deformation. Extensional features are located in three main regions also located around the periphery but closer to the center of the Tharsis bulge: the northeast region with the western part of Tempe Terra, the northwest region with Acheron Fossae and the south and southeast region with Claritas Fossae and Thaumasia Planum (Fig. 5). The majority of these normal faults are short (<300 km). Compressional features (<200 km) are concentric to Tharsis and are located in two peripheral regions: the eastern part of Tempe Terra with a small number of faults and Thaumasia Planum in the southeast region (Fig. 6).

Stage 3

The Early Hesperian stage is characterized both by a peak of extensional (between 1×10^{-4} and 2×10^{-4} km/Myr/km^2) and compressional (between 5×10^{-5} and 1×10^{-4} km/Myr/km^2) deformation. Extensional features are located in three main regions: the northeast region with Tempe Terra (Ascuris Planum), the east region with Valles Marineris and Lunae Planum and the center-north region with Ceraunius, Ulysses and Uranius Fossae (Fig. 5). Most of the normal faults are short (<300 km) but their length can reach 400–600 km, especially in Tempe Terra. The peak of compressional deformation is located in the southern part of Tempe Terra, Lunae and Solis Planum and the northern part of Xanthe Terra. The majority of the wrinkle ridges are short (<200 km) but their length can reach 400 km in Solis Planum and in Lunae Planum (Fig. 6).

Stage 4

The stage 4 (Late Hesperian) is characterized both by declining extensional (between 2.7×10^{-5} and 5.7×10^{-5} km/Myr/km^2) and compressional (between 1.6×10^{-5} and 8×10^{-6} km/Myr/km^2) deformation. The extensional features affect mostly the Late Hesperian volcanic unit (lHv), and the Valles Marineris region. In details, the deformed units are located in Noctis Labyrinthus and Fossae, in the western part of Solis Planum and in three windows (Tractus, Ulysses and Fortuna fossae) covered by Amazonian and Hesperian volcanic units (Fig. 5). The extensional features located in the lHv unit (late Hesperian volcanic) can be up to 400 km in length. The compressional features (Fig. 6) are peripheral and located in the south in Sinai and Solis Planum and in the east (Chryse Planitia and east of Lunae Planum).

Stage 5

The tectonic deformation largely declined during the Early Amazonian and is mainly extensional. The extensional features (Fig. 5) affect mostly the Amazonian and Hesperian volcanic unit (AHv) defined by Tanaka et al. (2014). This unit is considered to be an early Amazonian unit in this study because cumulative crater densities described by Tanaka et al. (2014) for this unit are close to the cumulative crater densities of other early Amazonian units as Early Amazonian basin unit (eAb). The extensional features affect also other Early Amazonian units AHi, Ave, AHtu, ANa. The AHv unit largely covers the surface of the Tharsis dome. Radial extensional features expand over the dome but are mostly concentrated in the Alba Patera region. These faults are the longest tectonic features on the Tharsis dome with lengths reaching more than 1000 km. The compressional features are peripheral and mainly located in the north around Alba Patera. Several compressional and extensional features are also observed in the south of Daedalia Planum and in Uranius Dorsum region close the Kasei Valles source (Fig. 6).

Stage 6

The tectonic deformation is very low during the Middle and Late Amazonian and is mainly extensional. Normal faults are observed in the Amazonian apron unit (Aa) and are related to the Olympus Mons formation. Several normal faults are also located in the late Amazonian apron unit (lAa) located in the western part of Arsia and Pavonis Mons (Fig. 5). Several compressional faults are also located on the flanks of Arsia Mons.

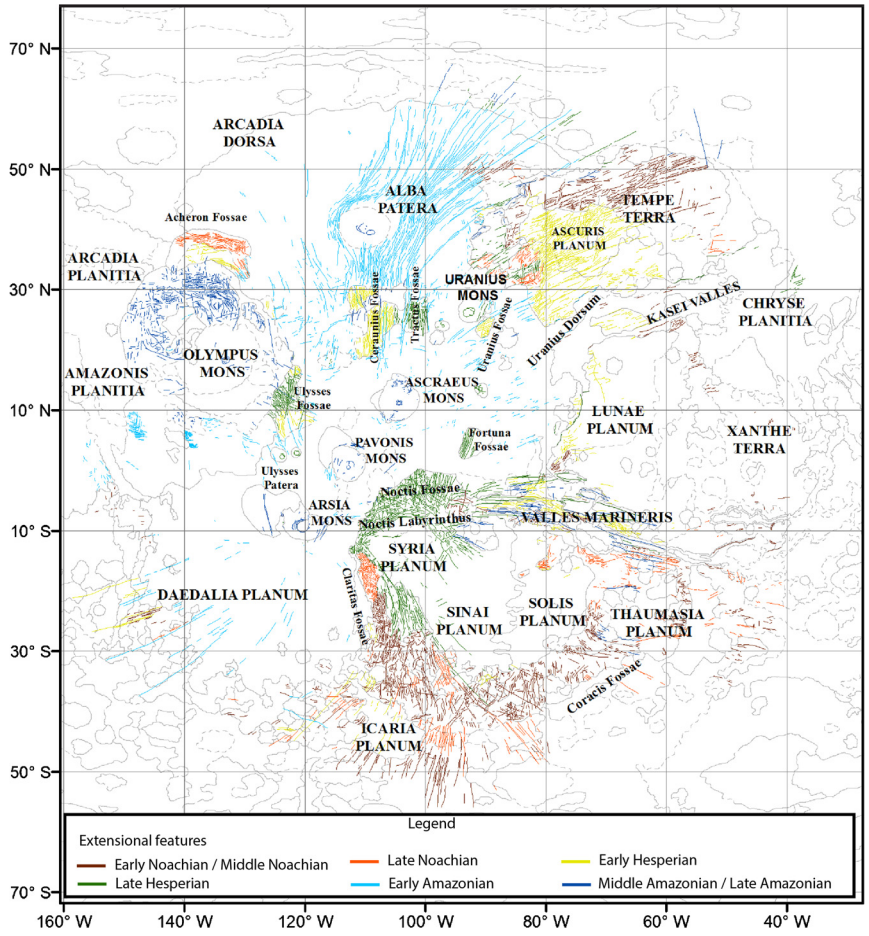

Fig. 5. Map of extensional features in the Tharsis region with color-coded ages.

4. Discussion

This study presents a new paleotectonic synthesis of the Tharsis dome. Judging by the number or length of tectonic features, linear fault density and deformation rate affecting exposed geological units of various ages, Tharsis-related activity began during the Noachian, but we found evidence for protracted tectonic activity. In contrast with previous studies (Anderson et al., 2001), we find that tectonic deformation was prolongated during the entire Hesperian and Early Amazonian periods with indicators of compression and extension rates reaching their maximum during Late Noachian and Early Hesperian. It is concluded that the compressional tectonic activity became significant in stage 2 (Middle/Late Noachian), prolongated in the Early Hesperian (stage 3). It mostly ceased in the Late Hesperian (stage 4) but some activity persisted until the early Amazonian. Compressional deformation is mostly characterized by peripheral wrinkle ridges in the eastern part of the Tharsis region, and appears to have migrated with time closer to the Tharsis center (East of Tempe Terra and Thaumasia Planum – stage 2 to the West of Tempe Terra and Solis Planum – stage 3). This migration could be a real evolution in the tectonic or might be an effect of the spatial distribution of units of different age. Judging by the fault density, the amount of extensional deformation seems to increase with time to peak in the stage 3 (Early Hesperian) and decline during the Late Hesperian and Amazonian. These observations shift the Tharsis tectonic activity by ∼100 Myr from the Noachian to the Early Hesperian. This revision is explained in part by the fact that the extensional features observed in Ceraunius and Uranius Fossae, Noctis Fossae and in a part of Tempe Terra were considered as Noachian by Anderson et al. (2001) whereas they cross-cut Early and Late Hesperian Terrains according to the recent map of Tanaka et al. (2014). Actually, the ages of these structures were considered to be possibly Early Hesperian by Anderson et al. (2001), despite being finally assigned to the Noachian stage in their statistics. This shift by ∼100 Myr, while seemingly small in the sense of absolute time, is very important relative to the overall evolution of Mars. Consequently, the growth of the Tharsis bulge is contemporary to the valley network formation (Bouley and Craddock, 2014) and its peak of activity during the Hesperian could influence the shift from phyllosilicate to sulfate formation at the Noachian–Hesperian boundary.

This tectonic history may be used to decipher the crustal growth of Tharsis as a function of time. The stress pattern around Tharsis depends on the mode of support of the topography of Tharsis. The mode of support can be either isostatic compensation (existence of a crustal root of lower density with respect to mantle density), flexural uplift (elastic deformation of the lithosphere due to stresses exerty by a buoyant interior) or surface load (elastic deformation of the lithosphere due to the load resulting from the accumulation of basaltic flows) (Banerdt et al., 1982). Stress distributions in the lithosphere were calculated for compensated and flexural modes using the equations of the thick shell theory (Banerdt et al., 1982). Comparison between model predictions and tectonic observations available at this time (Scott and Carr, 1978) suggest a three-phase model, where isostatic compensation is followed by two stages of flexural loading. Our observations remain consistent with a formation dominated by extrusive and intrusive volcanism accommodated by lithospheric flexure, but occurring over a more extended period of time with a major phase in the Early Hesperian. This scenario is consistent with a Hespe-

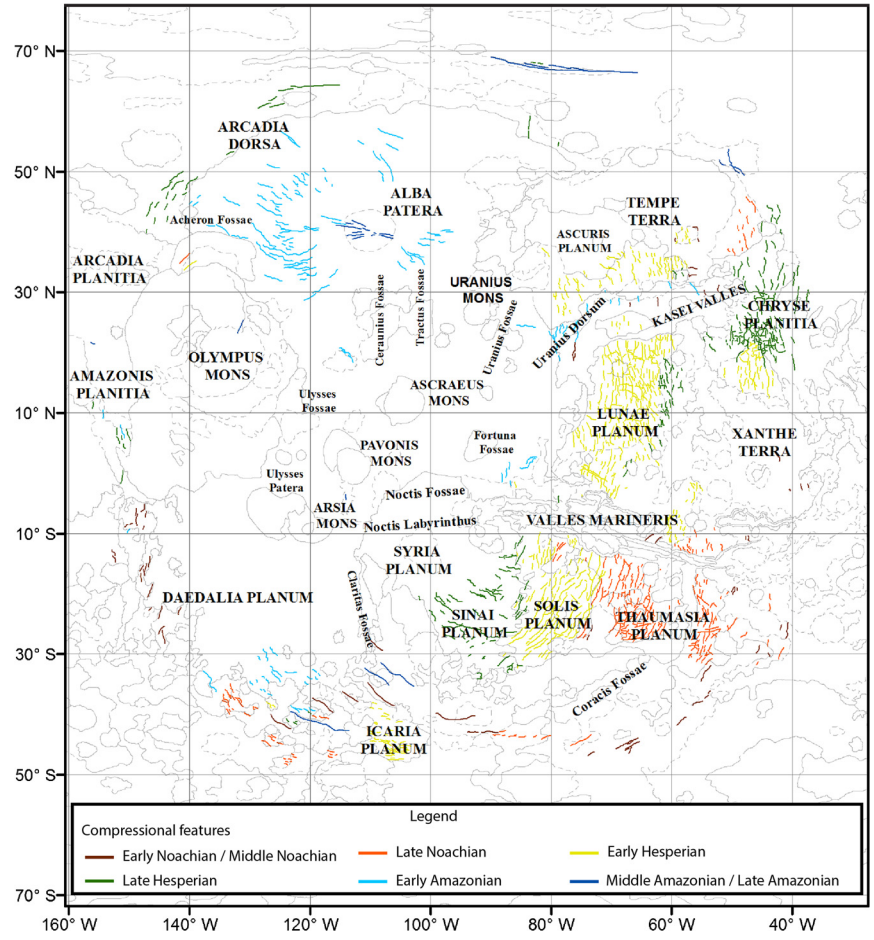

Fig. 6. Map of compressional features in the Tharsis region with color-coded ages.

rian Tharsis-driven true polar wander, as argued by Bouley et al. (2016) from the distribution of valley networks. Precise comparison of the results of these independent approaches would require a better knowledge of the mode of construction of Tharsis as a function of time, since larger variation of the inertia tensor would be produced by a flexural uplift than isostatic compensation. Indeed, isostatic compensation may be achieved through internal differentiation, producing a low density material and a dense residual, where the mass of the entire column can be preserved, whereas flexural deformation involves the addition (flexural loading) or removal (flexural uplift) of mass to that column.

Several issues may be examined to refine further this tectonic scenario. It is of note that the timing of wrinkle ridge deformation was likely modulated by global stresses due to planetary cooling and contraction (Mangold et al., 2000), even though the concentric pattern around Tharsis is clearly influenced by Tharsis. Despite Mangold et al. (2000) suggesting a global contraction event occurring essentially in the Late Hesperian, we cannot exclude that some wrinkle ridges are related to these global stresses and contribute to the observed compression peak.

A more in-depth interpretation of cumulative fault length shall consider the tectonic style which may vary between stage and may not be systematically related to lithospheric loading. For instance, extensional faults formed during the Early Hesperian to Early Amazonian are longer than in the Noachian. Many of the later extensional structures are associated with graben interpreted as overlying giant dike swarms, which are naturally quite long (Mège and Masson, 1996). Furthermore, a large part of Noachian tectonic features are located in Claritas and Coracis Fossae and Thaumasia Planum. Wilson and Head (2002) and Mège (2003) suggested that these structures are part of a giant Tharsis-radial graben system and could be the surface manifestation of mantle plume-related dike intrusion complexes. Alternatively, several authors have interpreted the topography of this region as localized pre-Tharsis "orogenic belts" (Anguita et al., 2001, 2006; Dohm et al., 2009; Nahm and Schultz, 2010), following the seminal ideas of Courtillot et al. (1975). Therefore, the idea that high elevations of Thaumasia highlands and Claritas Fossae, clearly acquired in the Noachian, could be extrapolated to the rest of the Tharsis region is not necessarily supported. These extensional fractures then might be not related to Tharsis, and do not have implications for constraining the timing of the emplacement of the Tharsis load. However, other more scattered extensional features related to Tharsis formation are observed in the Tempe Terra region that prove that tectonic activity began in the Noachian at the periphery of the dome.

Other limitations arise from uncertainties about the ages of tectonic features. Further investigations may help to constrain the intensity of the tectonic activity as a function of time. For instance, the Noachian age of the tectonic features in Tempe Terra may be confirmed using the buffered crater counting technique (Kneissl et al., 2015). If successful on Tempe Terra, this approach may be applied to the whole Tharsis region to provide more precise ages compared to the conventional stratigraphic approach. Measuring the maximal displacement on the different faults with high-resolution Digital Elevation Models could also help to compare quantitatively the intensity of deformation affecting the different units. High-resolution data might be also useful to identify the reactivation of ancient faults in more recent tectonic context, which is ignored in past studies.

5. Conclusion

Our analysis of tectonic features related to Tharsis based on the revised ages of the several geological units by Tanaka et al. (2014) implies a significant revision of the tectonic history of Tharsis. We find that the tectonic deformation extended from the Noachian through the Amazonian, with extensional and compressional activity peaking in the Late Noachian to Early Hesperian. Since deformation is related to crustal growth either in response to isostatic uplift and flexural loading of Tharsis, we conclude that Tharsis has several major growth phases or a single prolonged growth phase from the Late Noachian to the Amazonian. This scenario is consistent with a Hesperian reorientation of Mars that moves Tharsis to its present equatorial position (Bouley et al., 2016). Far-reaching consequences of a protracted growth of Tharsis on the evolution of the topography of Mars should be carefully estimated by numerical simulations and considered as a new framework for geological studies of early Mars.

Acknowledgement

The authors thank Martin Knapmeyer for providing the extended global catalog of mars surface faults. This research was funded by the GEOPS laboratory and the Programme National de Planétologie of INSU-CNRS.

Appendix A. Supplementary material

Supplementary material related to this article can be found online at https://doi.org/10.1016/j.epsl.2018.02.019. These data include the Google map of the most important areas described in this article.

References

Anderson, R.C., Dohm, J.M., Golombek, M.P., Haldemann, A.F.C., Franklin, B.J., Tanaka, K.L., Lias, J., Peer, B., 2001. Primary centers and secondary concentrations of tectonic activity through time in the western hemisphere of Mars. J. Geophys. Res. 106 (E9), 20563. https://doi.org/10.1029/2000JE001278.

Anguita, F., Farelo, A.-F., López, V., Mas, C., Muñoz-Espadas, M.-J., Márquez, Á., Ruiz, J., 2001. Tharsis dome, Mars: new evidence for Noachian–Hesperian thick-skin and Amazonian thin-skin tectonics. J. Geophys. Res. 106 (E4), 7577. https://doi.org/10.1029/2000JE001246.

Anguita, F., Fernández, C., Cordero, G., Carrasquilla, S., Anguita, J., Núñez, A., Rodríguez, S., García, J., 2006. Evidences for a Noachian–Hesperian orogeny in Mars. Icarus 185 (2), 331–357. https://doi.org/10.1016/j.icarus.2006.07.026.

Banerdt, W.B., Phillips, R.J., Sleep, N.H., Saunders, R.S., 1982. Thick shell tectonics on one-plate planets: application to Mars. J. Geophys. Res. 87, 9723–9733.

Banerdt, W.B., Golombek, Matthew P., Tanaka, Kenneth L., 1992. Stress and tectonics on Mars. Lunar and planetary exploration. In: Mars (A93-27852 09-91), pp. 249–297.

Bouley, S., Craddock, R.A., 2014. Age dates of valley network drainage basins and subbasins within Sabae and Arabia Terrae, Mars. J. Geophys. Res., Planets 119 (6), 1302–1310.

Bouley, S., Baratoux, D., Matsuyama, I., Forget, F., Séjourné, A., Turbet, M., Costard, F., 2016. Late Tharsis formation and implications for early Mars. Nature 531, 7592.

Carr, M.H., Head, J.W., 2010. Geologic history of Mars. Earth Planet. Sci. Lett. 294 (3–4), 185–203. https://doi.org/10.1016/j.epsl.2009.06.042.

Courtillot, V.E., Allegre, C.J., Mattauer, M., 1975. On the existence of lateral relative motions on Mars. Earth Planet. Sci. Lett. 25, 279–285. https://doi.org/10.1016/0012-821X(75)90242-3.

Dohm, J.M., Tanaka, K.L., 1999. Geology of the Thaumasia region, Mars: plateau development, valley origins, and magmatic evolution. Planet. Space Sci. 47 (3–4), 411–431. https://doi.org/10.1016/S0032-0633(98)00141-X.

Dohm, J.M., Ferris, J.C., Baker, V.R., Anderson, R.C., Hare, T.M., Strom, R.G., Barlow, N.G., Tanaka, K.L., Klemaszewski, J.E., Scott, D.H., 2001. Ancient drainage basin of the Tharsis region, Mars: potential source for outflow channel systems and putative oceans or paleolakes. J. Geophys. Res. 106 (E12), 32943. https://doi.org/10.1029/2000JE001468.

Dohm, J.M., Anderson, R.C., Williams, J.-P., Ruiz, J., McGuire, P.C., Buczkowski, D.L., Wang, R., Scharenbroich, L., Hare, T.M., Connerney, J.E.P., Baker, V.R., Wheelock, S.J., Ferris, J.C., Miyamoto, H., 2009. Claritas rise, Mars: pre-Tharsis magmatism? J. Volcanol. Geotherm. Res., 139–156.

Ehlmann, B.L., Anderson, F.S., Andrews-Hanna, J., Catling, D.C., Christensen, P.R., Cohen, B.A., Dressing, C.D., Edwards, C.S., Elkins-Tanton, L.T., Farley, K.A., Fassett, C.I., Fischer, W.W., Fraeman, A.A., Golombek, M.P., Hamilton, V.E., Hayes, A.G., Herd, C.D.K., Horgan, B., Hu, R., Jakosky, B.M., Johnson, J.R., Kasting, J.F., Kerber, L., Kinch, K.M., Kite, E.S., Knutson, H.A., Lunine, J.I., Mahaffy, P.R., Mangold, N., McCubbin, F.M., Mustard, J.F., Niles, P.B., Quantin-Nataf, C., Rice, M.S., Stack, K.M., Stevenson, D.J., Stewart, S.T., Toplis, M.J., Usui, T., Weiss, B.P., Werner, S.C., Wordsworth, R.D., Wray, J.J., Yingst, R.A., Yung, Y.L., Zahnle, K.J., 2016. The sustainability of habitability on terrestrial planets: insights, questions, and needed measurements from Mars for understanding the evolution of Earth-like worlds. J. Geophys. Res., Planets 121 (10), 1927–1961.

Hartmann, W.K., 2005. Martian cratering 8: isochron refinement and the chronology of Mars. Icarus 174 (2), 294–320.

Ivanov, B.A., 2001. Mars/Moon cratering rate ratio estimates. Space Sci. Rev. 96, 87–104.

Knapmeyer, M., Schneider, S., Misun, M., Wählisch, M., Hauber, E., 2008. An extended global Inventory of Mars Surface Faults. In: European Geosciences Union – General Assembly. Vienna (Austria), April 13–18, 2008.

Kneissl, T., Michael, G.G., Platz, T., Walter, S.H.G., 2015. Age determination of linear surface features using Biffered Crater Counting Approach – case studies of the Sirenum and Fortuna Fossae graben systems on Mars. Icarus 250, 384–394.

Mangold, N., Allemand, P., Thomas, P.G., Vidal, G., 2000. Chronology of compressional deformation on Mars: evidence for a single and global origin. Planet. Space Sci. 48, 1201–1211.

Mège, D., Masson, P., 1996. A plume tectonics model for the Tharsis province, Mars. Planet. Space Sci. 44 (12), 1499–1546.

Mège, D., 2003. Volcanic rifting at martian grabens. J. Geophys. Res. 108 (E5), 5044. https://doi.org/10.1029/2002JE001852.

Morris, E.C., Tanaka, K.L., 1994. Geologic maps of the Olympus Mons region of Mars. U.S. Geol. Surv. Misc. Invest. Ser., Map 1-2327-B.

Nahm, A.L., Schultz, R.A., 2010. Evaluation of the orogenic belt hypothesis for the formation of the Thaumasia Highlands, Mars. J. Geophys. Res. 115, E04008. https://doi.org/10.1029/2009JE003327.

Phillips, R.J., Zuber, M.T., Solomon, S.C., Golombek, M.P., Jakosky, B.M., Banerdt, W.B., Smith, D.E., Williams, R.M., Hynek, B.M., Aharonson, O., Hauck, S.A., 2001. Ancient geodynamics and global-scale hydrology on Mars. Science 291, 2587–2591.

Scholz, C.H., 1982. Scaling laws for large earthquakes: consequences for physical models. Bull. Seismol. Soc. Am. 72, 1–14.

Scott, D.H., Carr, M.H., 1978. Geological map of Mars. Map I-1083. U.S. Geol. Surv., Reston, VA.

Scott, D.H., Tanaka, K.L., 1986. Geologic map of the western equatorial region of Mars, 1986. Scale 1:15,000,000. U.S. Geol. Surv. Misc. Invest. Ser., Map I-1802-A.

Scott, D.H., Dohm, J.M., 1990. Faults and ridges: historical development in Tempe Terra and Ulysses Patera regions of Mars. Proc. Lunar Planet. Sci. Conf. 20, 503–513.

Tanaka, K.L., Davis, P.A., 1988. Tectonic history of the Syria Planum Province of Mars. J. Geophys. Res. 93, 14,893–14,917.

Tanaka, K.L., 1990. Tectonic history of the Alba Patera–Ceraunius Fossae region of Mars. Proc. Lunar Planet. Sci. Conf. 19, 515–523.

Tanaka, K.L., Skinner, J.A.J., Dohm, J.M., Irwin, R.P., Kolb, E.J., Fortezzo, C.M., Platz, T., Michael, G.G., Hare, T.M., 2014. Geologic map of Mars. In: U.S. Geological Survey Scientific Investigations Map 3239, Scale 1:20,000,000, p. 43.

Viviano-Beck, C.E., Murchie, S.L., Beck, A.W., Dohm, J.M., 2017. Compositional and structural constraints on the geologic history of eastern Tharsis Rise, Mars.

Werner, S.C., Tanaka, K.L., 2011. Redefinition of the crater-density and absolute-age boundaries for the chronostratigraphic system of Mars. Icarus 215, 603–607. https://doi.org/10.1016/j.icarus.2011.07.024.

Wilson, L., Head, J.W., 2002. Tharsis-radial graben systems as the surface manifestation of plume-related dike intrusion complexes: models and implications. J. Geophys. Res. 107, 5057–5081.

Wise, D.U., Golombek, M.P., McGill, G.E., 1979. Tharsis Province of Mars – geologic sequence, geometry, and a deformation mechanism. Icarus 38, 456–472.

Witbeck, N.E., Tanaka, K.L., Scott, D.H., 1991. Geologic map of the Valles Marineris region. Mars IMAP-2010. USGS.